Dalton Transactions

Tin oxide subnanoparticles: a precisely-controlled synthesis, subnano-detection for their detail characterisation and applications

Journal:	*Dalton Transactions*
Manuscript ID	DT-FRO-06-2020-002186.R1
Article Type:	Frontier
Date Submitted by the Author:	20-Jul-2020
Complete List of Authors:	Kuzume, Akiyoshi; Tokyo Institute of Technology, Institute of Innovative Research Yamamoto, Kimihisa; Tokyo Institute of Technology, Chemical Resources Laboratory

ARTICLE

Tin oxide subnanoparticles: a precisely-controlled synthesis, subnano-detection for their detail characterisation and applications

Received 00th January 20xx,
Accepted 00th January 20xx

DOI: 10.1039/x0xx00000x

Akiyoshi Kuzume, Kimihisa Yamamoto*

Subnanometric metal particles exhibit anomalous chemical activity, suggesting innovative applications as next-generation materials. However, a precise synthesis and detail characterisation of these subnano-materials remains a major challenge. Here we summarise recent works on the synthesis of size-controlled tin (Sn) oxide subnanoparticles (SNPs) using the dendrimer template method, and on their detailed characterisation. Size-controlled Sn oxide SNPs (Sn_{12}, Sn_{28} and Sn_{60}) have been synthesised and showed a size-dependent composition change containing not only stable Sn(IV) states but also metastable Sn(II) states so as to form subnano-scaled particle shapes. Detailed vibrational characterisation of SNPs was achieved by establishing subnano-sensitive Raman spectroscopy for spectroscopic characterisation. Combined with density functional theory studies, the inherent subnano-structures of the Sn oxide SNPs has been elucidated for the first time. Furthermore, the size-dependent activity of Sn oxide SNPs on the CO oxidation was rationally explained from the simulated structure of Sn oxide SNPs. A detailed understanding of the chemical and physical nature of subnano-materials facilitates the rational design of SNPs for practical applications such as catalysis, biosensors, and electronics.

Introduction

Nanomaterials are one of the most widely investigated substances in innovative research and development studies within numerous scientific fields with varieties of potential applications, such as catalysts, electronics, optics, sensors and biomedical applications. In particular, nanomaterials made of metals, semiconductors and oxides are of great interest for electrical, optical, chemical, magnetic and other properties, that are distinctively different from that of bulk materials. What makes nanomaterial special here is that their properties mentioned above vary significantly with their size, while a bulk material has constant physical properties regardless of its size. For instance, semiconductor nanoparticles show quantum confinement effect, and coinage metals in nanoscale induce surface plasmon resonance. Therefore, there have been many studies aimed at the production of homogeneous nanocrystals with fine control of the size and shape so as to tune their physical, chemical and electrical properties. Recently, there has been a breakthrough in the fabrication of monodisperse nanocrystals in the size range around 1 nm in diameter: so-called subnano-particles (SNPs)[1-2]. SNPs exhibit discrete characteristics with respect to the number of constituent atoms (atomicity), such as unexpectedly high catalytic activity in the electrochemical reduction of oxygen[3-6], hydrogenation of olefin[7], and the aerobic oxidation of hydrocarbons[8-10], as well as a quantum size effect with notable shifts in bandgap energy with atomicity[11]. However, a detailed understanding of the physical and chemical properties of SNPs is still in its early stage. In the realm of nanomaterials, one of the most intriguing materials is tin (Sn) oxide. Since it is inexpensive and abundant, intensive research has been conducted on a wide range of applications for Sn oxide nanoparticles such as gas sensor, (electro)chemical catalysts, and transparent conductors. In addition, Sn oxide nanoparticles deposited on supports have gained much attention as the heterogeneous catalysis, providing fundamental insight into the specific reaction mechanism. Recent studies have shown that Sn oxide catalysts have different stoichiometry, Sn(II) and Sn(IV), depending on their physical structure such as size, crystallographic planes, morphology, surface composition, and density of defect sites[12-15]. In general, Sn(IV) is a thermodynamically stable phase, while Sn(II) is a metastable one in the bulk crystals[16-18]. The emergence of the Sn(II) components in Sn oxide nanoparticles is caused by the formation of oxygen vacancies on the surface; i.e. a crystal structure of SnO_2 (Sn(IV)) is in the classical rutile type structure which cannot be maintained its structure in nanoparticles that have high surface curvature, and thus it is more energetically favourable to partially include Sn(II) sites on the surface of nanoparticles[19-23]. Because of the low oxygen-vacancy-formation energy where their surface is easily reduced from Sn(IV) to Sn(II) depending on the oxygen partial pressure in the atmosphere[24-26], SnO_2 is known to be effective catalysts for CO oxidation reaction. The CO oxidation over the surface of Sn oxide proceeds based on the Mars-van-Krevelen mechanism, in which the reduction and the oxidation of Sn atoms occur on

JST-ERATO, Yamamoto Atom Hybrid Project, Tokyo Institute of Technology, Yokohama 226-8503, Japan.
E-mail: yamamoto.k.at@m.titech.ac.jp

the surface[27]. The common understanding is that partially reduced Sn(II) species on the surface are the active sites for CO oxidation reaction, where Sn(II) species act as an electron donor to transfer electrons to oxygen molecules adsorbed on the surface to generate active oxygen species attacking adjacent CO molecules in the reaction cycle. However, the correlation between the surface stoichiometry and the oxidation activity is obscure.

Herein, we summarise our recent works on the precise synthesis of Sn oxide SNPs with different size, a fundamental understanding of their physical characteristics, development of a spectroscopic technique to reveal chemical information and detail structural natures of Sn oxide SNPs, as well as on the elucidation of their catalytic activity and mechanism towards CO oxidation[28,29]. Finally, we provide a comprehensive understanding of the chemical and structural natures of Sn oxide SNPs that rationally explain their specific size-dependent catalytic activity during the CO oxidation reaction.

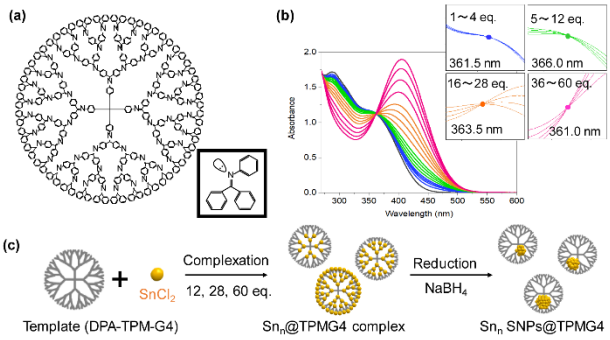

Fig. 1 (a) Molecular structure of DPA-TPM-G4. Inset: imine part at where Lewis acid is attracted. (b) UV-vis spectral titration, monitoring the accumulation process of $SnCl_2$, showing four isosbestic points (inset) due to the stepwise accumulation within the dendrimer molecule. (c) The preparation process of Sn oxide SNPs via a dendrimer template method. Reprinted from ref. 29 with permissions. Copyright AAAS (2019).

Synthesis of the Sn oxide SNPs

The precise preparation of SNPs is realised by using nano-synthesizers, in which a precise number of metal complexes is first accumulated at the coordinating sites within the dendrimer molecules. Subsequently, multinuclear-complexed dendrimer molecules were chemically reduced to form a size-monodispersed metal particle within the template molecule[1]. This approach, a dendrimer template method, is extremely general and widely applicable to many of the metallic elements in the periodic table[30]. Sn oxide SNPs were prepared by our original template technique using the fourth-generation dendritic phenylazomethine[31] with a tetraphenylmethane core (DPA-TPM-G4) as a template molecule (Fig. 1a)[32], which is composed of a π-conjugated rigid skeleton and 60 of intramolecular imine moieties (inset of Fig. 1a), a typical Schiff base, that can coordinate with Lewis acidic species to form a multinuclear complex as a precursor of a SNP[1,2]. In this technique, potential gradient properties of dendrimer molecules induce the stepwise accumulation of metal complexes from the inner generation layers towards the outer generation layers during the titration of metal salts. This accumulation process can be monitored by the UV-vis spectral titration (Fig. 1b). UV-vis absorption spectra of DPA-TPM-G4 upon stepwise addition of $SnCl_2$ showed gradual spectral change due to the one-to-one coordination with the imine nitrogen atoms, exhibiting four isosbestic point in turn (inset of Fig. 1b). Each respective generation layer consists of 4, 8, 16 and 32 imine sites, and a gradual multistep complexation process allows the formation of stable monodispersed complexes containing 4, 12, 28 and 60 metal atoms, respectively, which offers precise size control (Fig. 1c). The presence of four isosbestic points was the evidence that the complexation proceeds in four steps. Furthermore, the each added amount of $SnCl_2$ until the switching of isosbestic points were in good agreement with the number of imine nitrogen atoms in each generation. Thus, it is suggestive that Sn ions were accumulated in a stepwise manner from the inner layer to the outer layer of the dendrimer template molecules[1,2]. After chemical reduction of precursors by $NaBH_4$ solution, the reaction solution including Sn oxide SNPs was casted either on the silicate film deposited on the commercial TEM grid for STEM observation or on the silicate substrate for AFM measurements for further structural analyses. They were later rinsed gently by water and chloroform to remove dendrimer and by-products, such as NaCl. For catalysis studies, Sn-dendrimer complexes were mixed with mesoporous silica (MPS) before $NaBH_4$ reduction, followed by the calcination at 600°C in air to oxidise Sn and remove dendrimer[28]. The absence of dendrimer and by-products was confirmed by the disappearance of Cl 2*p* and N 1*s* core level signals in X-ray photoelectron spectra[28].

Characterisation of Sn oxide SNPs

Structural analysis by a high-angle annular dark-field scanning transmission electron microscopy (HAADF-STEM) found that the size of Sn_{12}, Sn_{28} and Sn_{60} oxide SNPs were around 0.9, 1.0 and 1.8 nm, respectively (Figs. 2a-c). These results from STEM observation agreed well with the trend determined by atomic force microscopic (AFM) study[29]. The SNPs have different sizes depending on the amount of $SnCl_2$ added to DPA-TPM-G4. Energy-dispersive X-ray spectroscopy (EDX) and elemental mapping also showed homogeneous distribution of Sn oxide SNPs over the silicate substrate[28].

The oxidation states of the Sn atoms and the composition of the Sn oxide SNPs were determined by Sn $3d_{5/2}$ core-level X-ray photoelectron spectroscopy (XPS) measurements (Figs. 2d-f)[28,29]. In each case, a significant contribution of a shoulder peak on the lower binding energy edge was apparent, indicating the

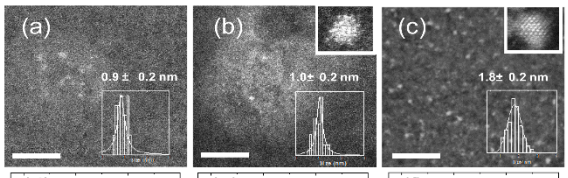

(g)		Binding Energy / eV		Peak area Ratio / %		
Atomicity	Preparation	Sn(IV)	Sn(II)	Sn(IV)	Sn(II)	Formula
Sn_{12}	Raw	487.6	484.6	41.2	58.8	$Sn_{12}O_{17}$
	Calcined	486.8	484.2	60	40	$Sn_{12}O_{19}$
Sn_{28}	Raw	487.3	484.5	49.7	50.3	$Sn_{28}O_{42}$
	Calcined	486.8	484.0	75	25	$Sn_{28}O_{49}$
Sn_{60}	Raw	486.6	484.1	66.3	33.7	$Sn_{60}O_{100}$
	Calcined	486.4	483.5	87	13	$Sn_{60}O_{112}$

Fig. 2 STEM images (a-c) and Sn $3d_{5/2}$ core-level XPS (d-f) of Sn_{12} (a,d), Sn_{28} (b,e) and Sn_{60} (c,f) oxide SNPs. (g) Size dependent Sn $3d$5/2 core-level XPS spectral parameters and estimated chemical formulae of Sn oxide SNPs. Reprinted and rearranged data reported in Supplementary materials in ref. 29 with permissions. Copyright AAAS (2019).

formation of sub-stoichiometric SnO_x ($1 < x < 2$) species intermediated between SnO and SnO_2. The spectra were deconvoluted into two peaks. The peak at higher binding energy at 486.4 – 487.6 eV corresponded to the Sn(IV) species[33,34], while that at lower binding energy at 483.5 - 484.6 eV were attributed to the Sn(II) species[35,36]. Stoichiometric compositions of Sn oxide SNPs could be estimated from the ratio of XPS peak intensity as $Sn_{12}O_{17}$ (x = 1.42), $Sn_{28}O_{42}$ (x = 1.50), $Sn_{60}O_{100}$ (x = 1.67) on silicate[29], and $Sn_{12}O_{19}$ (x = 1.58), $Sn_{28}O_{49}$ (x = 1.79), $Sn_{60}O_{112}$ (x = 1.87) on MPS after calcination (Fig. 2g)[28]. The proportion of Sn(II) in SNPs increased with decreasing the size, and that on the silicate surface was slightly higher than that loaded on MPS in which Sn oxide were calcined in air.

For a detailed comprehensive understanding of the chemical and structural states of Sn oxide SNPs, further spectroscopic characterisation is essential. However, the spectroscopic detection of subnano-scale substances is difficult in general because of a severely weak signal intensity, as well as the limited sensitivity and accuracy of conventional spectroscopic techniques. In addition, the surface coverage of SNPs on a support can be an issue. SNPs are not stable and readily aggregate if they are not supported or if the surface coverage is overly high on the support. Therefore, SNPs supported on carbon, silicate, graphene and other substrates must be at a concentration as low as 0.4 weight % to guarantee sufficient distance between adjacent SNPs, so as to avoid surface agglomeration[7]. As a consequence, the detection limit of conventional spectroscopic methods is far below the level required to detect isolated SNPs, and thus, it is extremely difficult to examine in detail the characteristics of subnano-substances.

Development of subnano-sensitivity Raman spectroscopy

Surface-enhanced Raman spectroscopy (SERS) is a powerful analytical technique capable of providing fingerprint information regarding the target substances. The vibrational signals associated with SERS are greatly enhanced in the presence of Au or Ag nanoparticles, which work as an optical amplifier. The sensitivity of SERS strongly depends on the size and shape of the amplifiers, as well as spatial design of the hotspots generated at the gaps between neighbouring nanoparticles. It is at these gaps that specific surface plasmon resonance phenomena emerges in response to the laser irradiation, which lead to a pronounced enhancement of the Raman signals. Therefore, a key aspect of obtaining high-sensitivity Raman signals is the successful design and fabrication of the plasmonic amplifiers.

We have introduced Ag-coated Au-core nanoparticles (Au@AgNPs) with a diameter of 100 nm as the optical amplifiers, synthesised via a seed-mediated multistep process (Fig. 3)[29]. The design of the Au@AgNPs were optimised by a theoretical study using a three-dimensional finite difference time domain (3D-FDTD) simulation (Fig. 3a)[37]. It can compute the electromagnetic field distribution and the enhancement characteristics of the hotspots for various materials and structural configuration. Au@AgNPs were further coated with the silica shells to form shell-isolated Au@Ag nanoparticles (Au@AgSHINs), inhibiting chemical and electrical interactions between SNPs and amplifiers such that only the intrinsic characteristics of the SNPs are assessed in the Raman spectrum (Fig. 3b)[38]. This configuration also allows using any type of substrates in terms of shape and materials, providing extensive applicability of this technique to interfacial analysis in the range

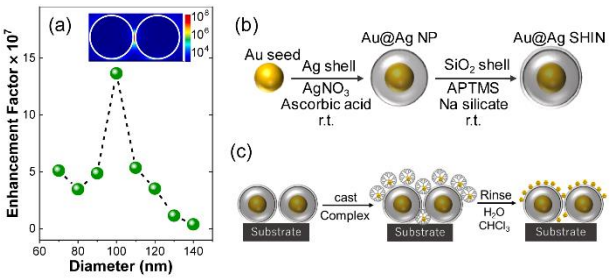

Fig. 3 (a) A simulation of the maximum size-dependent enhancement at the hotspot between two Au@AgSHINs as calculated by 3D-FDTD simulations. Schematic diagrams of (b) the synthesis of Au@AgSHIN and of (c) the sample preparation for SERS analyses of Sn oxide SNPs. (a) is reprinted from ref. 29 with permissions. Copyright AAAS (2019).

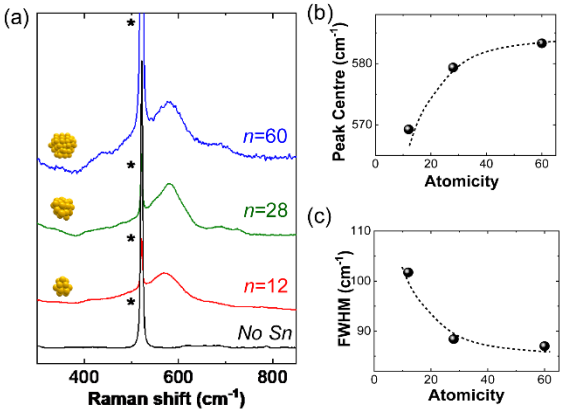

Fig. 4 (a) SERS spectra of Sn oxide SNPs casted on Au@AgSHINs on Si substrates, compared with a reference spectrum obtained without $SnCl_2$ as a blank. Effects of atomicity on (b) the peak position and (c) FWHM values. The Raman signal from the silicon substrate is indicated by an asterisk. Reprinted from ref. 29 with permissions. Copyright AAAS (2019).

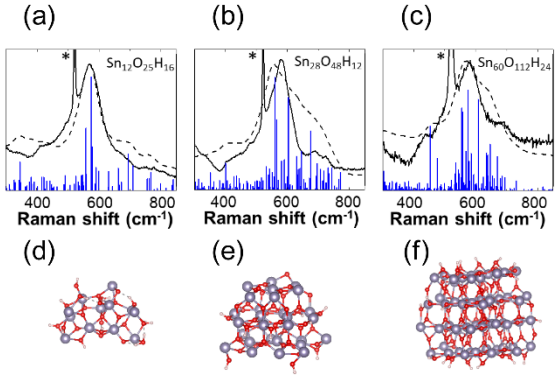

Fig. 5 (a)-(c) Experimental SERS spectra (solid line) and simulated spectra (dashed line) along with (d)-(f) the SNP structures simulated by DFT calculations after the structural optimisation process for (a,d) Sn_{12}, (b,e) Sn_{28} and (c,f) Sn_{60} SNCs. The Raman signal from the silicon substrate is indicated by an asterisk. Reprinted and rearranged data reported in the main text and Supplementary materials in ref. 29 with permissions. Copyright AAAS (2019).

from subnano to micro-scale. For Raman measurements of Sn oxide SNPs, SNPs were loaded on the Au@AgSHINs-coated Si substrates (Fig. 3c). EDX and elemental mapping analyses confirmed the presence of homogeneously distributed Sn on the Au@AgSHIN surfaces[29].

The SERS spectra of Sn oxide SNPs using Au@AgSHINs contained only a single intense but broad peak, with a maximum between 569 and 583 cm^{-1} (Fig. 4a). These broad peaks cannot be ascribed to any of the modes predicted by group theory[39-47]. In addition, the characteristic three Raman bands from the rutile-type SnO_2 were absent[39]. The emergence of a broad signal, in general, is typically indicative of the accumulation of signals from Sn-O bonds with slightly different binding configurations. Therefore, spectral observation on Sn oxide SNPs suggested the complete deformation of the crystalline structure of rutile type Sn oxide along with the formation of multi-atomic clusters with distorted atomic configurations. The position of the Raman peak maxima and the full-width at half-maximum (FWHM) values of the undefined peaks were directly acquired from the spectra and were plotted as functions of the constituent atomicity, respectively (Figs. 4b and 4c). A red-shift and broadening of the peak width with decreasing SNP size were apparent, indicating that the size, even at the subnano-scale, affects the spectral properties sensitively.

Structure simulation and vibrational analyses of Sn oxide SNPs

Further structural deliberation of the Sn oxide SNPs required ab initio theoretical calculations that simulate the vibrational features in Raman spectra based on the atomic configuration of model clusters[47]. For this purpose, density functional theory (DFT) calculations were performed, using model Sn oxide SNPs with stoichiometric composition estimated from XPS data (Fig. 2g). These models were constructed starting from a rutile-type crystal structure, which was subsequently geometrically optimised to obtain a minimum energy configuration. Vibrational spectra were then simulated based on the structures obtained for each model SNPs and compared to the experimental SERS spectra[29]. Since Sn oxide SNPs were exposed to air, water molecules were added to the stoichiometric formula obtained from XPS, adjusting the simulated vibrational spectra to the experimental spectra[48]. As a consequence, simulated spectra based on vibrational analyses accurately reproduced the spectral shapes observed in the experiments (Figs. 5a-c). The broad bands in the SERS spectra were blue-shifted by 10 to 30 cm^{-1} when Sn oxide SNPs were calcined[29]. The variations in the main peak position upon calcination therefore provide evidence for the presence of hydroxyl group in the SNPs[29].

The modification of atomic coordinates, such as the introduction of oxygen vacancies and hydroxyl species, is known to change the local morphology of SNPs, which, in turn, affects the corresponding vibrational features. Therefore, reproducing unique experimental Raman spectra by simulated vibrational analyses can corroborate these morphological parameters, providing further information regarding the structure-chemical activity correlation of Sn oxide SNPs towards CO oxidation.

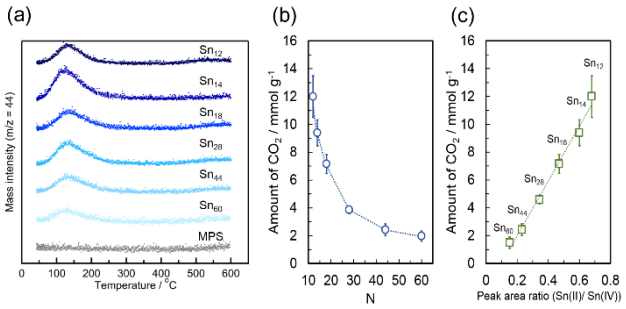

Fig. 6 (a) Typical CO-TPR spectra of Sn oxide SNPs for different size supported on MPS. The bare MPS as a control sample showed no significant peaks (grey dots), indicating MPS itself is inert to the CO oxidation in this temperature range. The amount of desorbed CO_2 from the Sn oxide SNPs estimated from the CO-TPR spectra as a function of (b) SNP size and of (c) the peak intensity ratio of the Sn(II) to the Sn(IV) from XPS measurements. Reprinted from ref. 28 with permissions. Copyright American Chemical Society (2018).

Size-dependent specific activity of Sn oxide SNPs towards CO oxidation

The CO oxidation reaction is one of the most simple oxidation reactions of industrial importance and seeks to eliminate CO from the reformed gas and exhaust-gas-catalysts, reducing CO poisoning of the catalyst[49]. To study the CO oxidation rates on Sn oxide SNPs with different size, we performed temperature-programmed reaction measurements using CO as a reacting gas (CO-TPR). The reactivity towards CO oxidation was evaluated by detecting CO_2 molecules generated during the reaction between the CO gas and adsorbed oxygen on the Sn oxide surface (Fig. 6a). The obtained CO-TPR spectra showed CO_2 peaks around 125-140°C for all the Sn oxide SNPs, while there was no signal for the blank MPS sample, confirming that the Sn oxide SNPs acted as the catalyst for the CO oxidation. As we already mentioned, the Sn oxide SNPs contained more electron-rich Sn(II) sites compared to bulk materials. The increase of Sn(II) sites leads to an increase in the surface charge density and lowering the reaction temperature[28]. High surface charge density decreases the activation energy of oxygen molecule dissociation into active atomic oxygen. In Fig. 6a, we found that the CO_2 production exponentially increased with decreasing the size of SNPs. The amount of produced CO_2 on Sn_{12} SNPs was 6.1 times higher than that on the Sn_{60} SNPs (Fig. 6b). We also plotted the amount of produced CO_2 molecules versus the composition of the Sn oxide SNPs calculated from XPS data, surprisingly showing a linear correlation (Fig. 6c). Estimating the CO oxidation activity of the Sn oxide SNPs by the amount of produced CO_2 molecules per weight, these results strongly suggest that Sn(II) is the active site of the SNPs.

The stoichiometric formulae of the Sn oxide SNPs obtained from the DFT simulations and Raman spectra were $Sn_{12}O_{25}H_{16}$, $Sn_{28}O_{48}H_{12}$ and $Sn_{60}O_{112}H_{24}$. A closer look at the optimised chemical structures of the model Sn oxide SNPs (Figs. 5d-f) revealed unique characteristics resulting from the structural distortion relative to the bulk crystals. A statistical analysis of all the Sn-O bond lengths in the simulated SNPs structures exhibited that the average bond length and the FWHM of the Sn-O length distribution curve both increased with decreasing SNP size (Fig. 7), in the same manner as the FWHM values of the broad peaks in the SERS spectra (Fig. 4c). Deviation from the bulk structure was more pronounced in the case of smaller SNPs, indicating that the Sn_{12} SNPs had a highly distorted atomic configuration with longer Sn-O bonds on average. Here, it is important to point out that the peak maxima in the SER spectra were red-shifted with decreases the size of SNPs (Fig. 4b). The red shift in Raman spectra indicate that the Sn-O bond strength in the SNPs decreased with decreasing size, which was consistent with the data showing elongation of the Sn-O bond with decreasing size (Fig. 7d). During CO oxidation, Sn oxide worked as oxygen donors, and so, it is likely that a lower Sn-O bond strength would promote bond cleavage to provide more oxygen species to enhance the CO oxidation process[28].

In addition, it is interesting to observe that all the Sn-O bonds longer than 0.22 nm were located at the edge of the SNPs, which represented the active sites for CO oxidation, and the content of surface hydroxyl groups was increased from Sn_{60} to Sn_{12}. Therefore, Sn oxide SNPs with 12 Sn atoms were found to have higher hydroxyl group coverage ratio and lower bond strengths. These results, as demonstrated via complementary approaches with the experimental SERS data and theoretical simulation, provided direct evidence to indicate the role of surface hydroxyl groups and with longer Sn-O bond, explaining

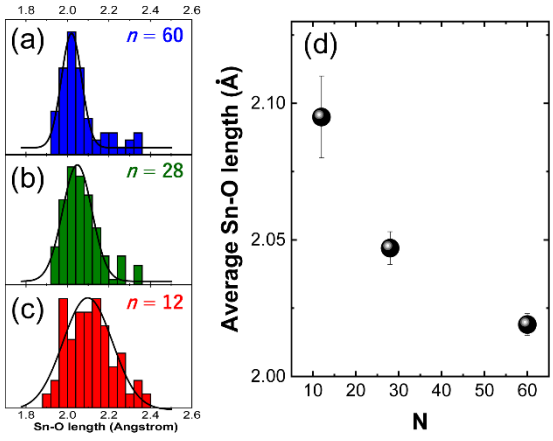

Fig. 7 (a) Histograms of the Sn-O bond length distribution estimated from the simulated structure of (a) $Sn_{60}O_{112}H_{24}$, (b) $Sn_{28}O_{48}H_{12}$, and (c) $Sn_{12}O_{25}H_{16}$. (d) Average Sn-O bond lengths as a function of atomicity. Reprinted and rearranged data reported in Supplementary materials in ref. 29 with permissions. Copyright AAAS (2019).

well the unusual oxidation activity of smaller SNPs during CO oxidation reaction.

Conclusions

We have synthesised size-controlled Sn oxide SNPs by employing the dendrimer template method. The synthesised Sn oxide SNPs unprecedentedly contained both stable Sn(IV) and metastable Sn(II) species, where the fraction of the latter increased with decreasing the size of SNPs. CO-TPR measurements revealed that the CO_2 production by the CO oxidation on Sn oxide SNPs increased with decreasing the size of SNPs, linearly correlating with the charge composition of the Sn atoms in the SNPs.

To elucidate the correlation between the chemical composition and reaction activity, subnano-sensitive Raman spectroscopic method was established, allowing the direct detection of the spectral features of subnano-scale materials, even at extremely low surface loadings, leading to a detailed comprehensive understanding of the chemical and structural states of Sn oxide SNPs. The spectra analyses of the unique Raman signals of Sn oxide SNPs were complemented by theoretical structural and vibrational analyses to assign the origin of the Raman characteristics of SNPs. The resulting structural and chemical information including the chemical formulae and structures of SNPs further rationally explained the specific size-dependent reaction activity of SNPs towards CO oxidation reaction.

These studies demonstrated the synthesis of subnano-scale materials of Sn oxide and their unprecedented size-dependent reaction activity towards CO oxidation as well as comprehensive understanding of chemical and structural natures of subnano-materials. It is important to emphasise the potential importance of our work on both the development of innovative subnano-materials as well as of subnano-sensitive analytical methodology. The development of subnano-sensitive spectroscopic technique allows the direct detection of the spectral features of subnano-materials for the first time, inducing a breakthrough of further precise technological developments at the atomic level in analytical chemistry. In addition, a detail understanding of physical and chemical nature of subnano-substances facilitates the rational design of subnano-materials on the atomic scale for practical application, and thus, accelerating material innovation and application studies at subnano-scale. As a consequence, our studies on Sn oxide SNPs inspired explorations in the field of subnano-science, promoting as an interdisciplinary research field.

Conflicts of interest

There are no conflicts to declare.

Acknowledgements

This work was supported by JST-ERATO (Grant number JPMJER1503) and JSPS KAKENHI Grant-in-Aid for Scientific Research (S) (Grant number 15H05757) as well as 17H05146, 17K14490 and 17K05896.

Notes and references

1 K. Yamamoto, M. Higuchi, S. Shiki, M. Tsuruta and H. Chiba, *Nature*, 2002, **415**, 509-511.
2 K. Yamamoto and T. Imaoka, *Acc. Chem. Res.*, 2014, **47**, 1127-1136.
3 K. Yamamoto, T. Imaoka, W.J. Chun, O. Enoki, H. Katoh, M. Takenaga and A. Sonoi, *Nat. Chem.*, 2009, **1**, 397-402.
4 T. Imaoka, H. Kitazawa, W.J. Chun and K. Yamamoto, *Angew. Chem. Int. Ed.*, 2015, **54**, 9810-9815.
5 M. Nesselberger, M. Roefzaad, R.F. Hamou, P.U. Biedermann, F.F. Schweinberger, S. Kunz, K. Schloegl, G.K.H. Wiberg, S. Ashton, U. Heiz, K.J.J. Mayrhofer and M. Arenz, *Nat. Mater.*, 2013, **12**, 919-924.
6 P. Bothra, M. Pandey and S.K. Pati, *Catal. Sci. Technol.*, 2016, **6**, 6389-6395.
7 T. Imaoka, Y. Akanuma, N. Haruta, S. Tsuchiya, K. Ishihara, T. Okayasu, W.J. Chun, M. Takahashi and K. Yamamoto, *Nat. Commun.*, 2017, **8**, 688.
8 S. Vajda, M.J. Pellin, J.P. Greeley, C.L. Marshall, L.A. Curtiss, G.A. Ballentine, J.W. Elam, S. Catillon-Mucherie, P.C. Redfern, F. Mehmood and P. Zapol, *Nat. Mater.*, 2009, **8**, 213-216.
9 M. Takahashi, H. Koizumi, W.J. Chun, M. Kori, T. Imaoka and K. Yamamoto, *Sci. Adv.*, 2017, **3**, e1700101.
10 M. Huda, K. Minamisawa, T. Tsukamoto, M. Tanabe and K. Yamamoto, *Angew. Chem. Int. Ed.,* 2019, **58**, 1002-1006.
11 N. Satoh, T. Nakashima, K. Kamikura and K. Yamamoto, *Nat. Nanotechnol.*, 2008, **3**, 106-111.
12 M. Foltin, G.J. Stueber and E.R. Bernstein, *J. Chem. Phys.* 1999, **111**, 9577-9586.
13 M. Nakayama, M. Xue, W. An, P. Liu and M.G. White, *J. Phys. Chem. C*, 2015, **119**, 14756-14768.
14 S. Vajda and M.G. White, *ACS Catal.*, 2015, **5**, 7152-7176.
15 J.A. Rodriguez, J. Graciani, J. Evans, J.B. Park, F. Yang, D. Stacchiola, S.D. Senanayake, S. Ma, M. Perez, P. Liu, J.F. Sanz and J. Hrbek, *Angew. Chem. Int. Ed.*, 2009, **48**, 8047-8050.
16 K. Nose, A.Y. Suzuki, N. Oda, M. Kamiko and Y. Mitsuda, *Appl. Phys. Lett.*, 2014, **104**, 091905.
17 Z.R. Dai, Z.W. Pan and Z.L. Wang, *J. Am. Chem. Soc.*, 2002, **124**, 8673-8680.
18 J. Geurts, S. Rau, W. Richter and F.J. Schmitte, *Thin Solid Films*, 1984, **121**, 217-225.
19 S. Ganguly Neogi and P. Chaudhury, *J. Comput. Chem.*, 2014, **35**, 51-61.
20 Z.W. Qu and G.L. Kroes, *J. Phys. Chem. C*, 2007, **111**, 16808-16817.
21 A. Iwaszuk, P.A. Mulheran and M. Nolan, *J. Mater. Chem. A*, 2013, **1**, 2515-2525.
22 M.J. Lundqvist, M. Nilsing, P. Persson and S. Lunell, *J. Quantum Chem.* 2006, **106**, 3214-3234.
23 M. Calatayud, L. Maldonado and C. Minot, *J. Phys. Chem. C*, 2008, **112**, 16087-16095.
24 C. Kilic and A. Zunger, *Phys. Rev. Lett.*, 2002, **88**, 095501.
25 I. Manassidis, J. Goniakowski, L.N. Kantorovich and M.J. Gillan, *Surf. Sci.*, 1995, **339**, 258-271.
26 W. Bergermayer and I. Tanaka, *Appl. Phys. Lett.*, 2004, **84**, 909-911.
27 P. Mars and D.W. van Krevelen, *Chem. Eng. Sci.*, 1954, **3**, 41-59.
28 Y. Inomata, K. Albrecht and K. Yamamoto, *ACS Catal.* 2018, **8**, 451-456.
29 A. Kuzume, M. Ozawa, Y. Tang, Y. Yamada, N. Haruta and K. Yamamoto, *Adv. Sci.*, 2019, **5**, eaax6455.

30 T. Tsukamoto, T. Kambe, A. Nakao, T. Imaoka and K. Yamamoto, *Nat. Commun*. 2018, **9**, 3873.
31 A. Kimoto, K. Masachika, J.S. Cho, M. Higuchi and K. Yamamoto, *Org. Lett.*, 2004, **6**, 1179-1182.
32 O. Enoki, H. Katoh and K. Yamamoto, *Org. Lett.* 2006, **8**, 569-571.
33 D. Dutta and D. Bahadur, *J. Mater. Chem.*, 2012, **22**, 24545-24551.
34 V. Kumar, V. Kumar, S. Som, J.H. Neethling, M. Lee, O.M. Ntwaeaborwa and H.C. Swart, *Nanotechnology*, 2014, **25**, 135701.
35 M. Mirzaee and A. Dolati, *J. Sol-Gel Sci. Technol.*, 2015, **75**, 582-592.
36 F.H. Aragón, J.A.H. Coaquira, I. Gonzalez, L.C.C.M. Nagamine, W.A.A. Macedo and P.C. Morais, *J. Phys. D: Appl. Phys.*, 2016, **49**, 155002.
37 V, Uzayisenga, X.D. Lin, L.M. Li, J.R. Anema, Z.L. Yang, Y.F. Huang, H.X. Lin, S.B. Li, J.F. Li and Z.Q. Tian, *Langmuir*, 2012, **28**, 9140-9146.
38 J.F, Li, Y.F. Huang, Y. Ding, Z.L. Yang, S.B. Li, X.S. Zhou, F.R. Fan, W. Zhang, Z.Y. Zhou, D.Y. Wu, B. Ren, Z.L. Wang and Z.Q. Tian, *Nature,* 2010, **464**, 392-395.
39 J.F. Scott, *J. Chem. Phys.*, 1970, **53**, 852-853.
40 M. Ocaña, C.J. Serna, J.V. Gracía-Ramos and E. Matijević, *Solid State Ionics*, 1993, **63-65**, 170-177.
41 J. Zuo, C. Xu, X. Liu, C.S. Wang, C.G. Wang, Y. Hu and Y. Qian, *J. Appl. Phys.*, 1994, **75**, 1835-1836.
42 K.N. Yu, Y. Xiong, Y. Liu and C. Xiong, *Phys. Rev. B*, 1997, **55**, 2666-2671.
43 L. Abello, B. Bochu, A. Gaskov, S. Koudryavtseva, G. Lucazeau and M. Roumyantseva, *J. Solid State Chem.*, 1998, **135**, 78-85.
44 A. Diéguez, A. Romano-Rodríguez, A. Vilà and J.R. Morante, *J. Appl. Phys.*, 2001, **90**, 1550-1557.
45 M.N. Rumyantseva, A.M. Gaskov, N. Rosman, T. Pagnier and J.R. Morante, *Chem. Mater.,* 2005, **17**, 893-901.
46 K. Vijayarangamuthu and S. Rath, *J. Alloys Compd.*, 2014, **610**, 706-712.
47 Density functional theory (DFT) calculations, for structural deliberation of Sn oxide SNCs to simulate vibrational features in Raman spectra, were performed with the BLYP functional and the LanL2DZ basis set for Sn as well as the 3-21G basis sets for H and O. Model clusters with stoichiometric compositions estimated from XPS data were first constructed by capturing from a rutile-type crystal structure. Later, water molecules were further added to the stoichiometric formula of each SNC. The constructed model clusters were geometrically optimised, with which then the vibrational analyses were performed. Based on the vibrational analyses, Raman scattering intensities for various resonance peaks were calculated (blue solid lines in Figs. 5a-c), and subsequently Raman spectra were simulated by adding a line width to each scattering intensity (black dashed curves in Figs. 5a-c). The line width was given by a Gaussian function with the half width of 30 cm^{-1}. Additionally, it should also be noted that a vibrational analysis usually gives a slight difference between the calculated vibrational frequencies and experimental ones, because of insufficient description of anharmonicity. It is, however, well known that such inaccuracy can be resolved by scaling the calculated frequencies. In the present study, a scaling factor 0.952 was employed, which was determined such that an experimental Raman spectrum of a rutile-type Sn oxide crystal is reproduced in a first-principles manner. For the crystal, periodic boundary conditions DFT calculations were carried out at the same level of theory as above. All the DFT calculations were conducted with the Gaussian 16, Rev. B.01 program package.
48 M. Ristić, M. Ivanda, S. Popović and S. Musicć, *J. Non-Crystalline Solids,* 2002, **303**, 270-280.
49 B.C.H. Steele and A. Heinzel, *Nature*, 2001, **414**, 345-352.

Tin oxide subnanoparticles: a precisely-controlled synthesis, subnano-detection for their detail characterisation and applications

Akiyoshi Kuzume, Kimihisa Yamamoto*

Table of Contents entry:

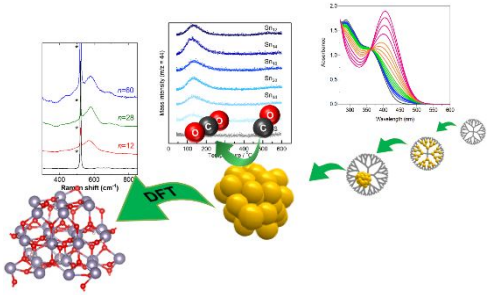

Precise synthesis, structural characterisation and application studies of atomicity-controlled tin oxide subnanoparticles